



Cite this: *RSC Adv.*, 2025, 15, 8456

# AIEE-driven highly sensitive fluorescent probe for Fe<sup>3+</sup> sensing in aqueous and solid phases: application in interference-free biological media†

Rida Khalid,<sup>a</sup> Tayyeba Javid,<sup>a</sup> Aqsa Pervaiz,<sup>a</sup> Mohammed A. Assiri,<sup>bc</sup> Zulfiqar Ali Khan,<sup>d</sup> Sania<sup>a</sup> and Sohail Anjum Shahzad \*<sup>a</sup>

Herein, a novel fluorescein-based fluorescent probe FHP was systematically designed and synthesised, which exhibited aggregation-induced emission enhancement (AIEE) properties. FHP showed the maximum emission response at a wavelength ( $\lambda_{\text{max}}$ ) of 516 nm. Using probe FHP, convenient and cost-effective sensing of Fe<sup>3+</sup> in solution and solid states was accomplished with notable sensitivity and selectivity. Quenching of the FHP fluorescence intensity was observed owing to the chelation between the electron-rich probe and electron-deficient Fe<sup>3+</sup>, with a detection limit of 253 nM. The FHP–Fe<sup>3+</sup> interaction was studied using UV-visible and fluorescence spectroscopies, dynamic light scattering (DLS), <sup>1</sup>H-NMR titration and density functional theory (DFT) calculations. Theoretical analysis was carried out using DFT to justify the non-covalent type of interaction in the FHP–Fe<sup>3+</sup> complex and to study the electronic properties of probe FHP and FHP–Fe<sup>3+</sup> complex. The practical application of the FHP probe in Fe<sup>3+</sup> sensing was evaluated using biological samples.

Received 3rd November 2024

Accepted 3rd March 2025

DOI: 10.1039/d4ra07824a

rsc.li/rsc-advances

## Introduction

Iron is an abundant transition metal found in the Earth's core, and it is one of the necessary micronutrients for almost all living beings.<sup>1</sup> It acts as a basic core for the structure and function of a variety of proteins such as haemoglobin (to carry oxygen in the body) and myoglobin (to ease the diffusion of oxygen in muscles).<sup>2</sup> Iron is also important for various cofactors that help in enzyme functioning and is a component of the prosthetic group in various enzymes,<sup>3</sup> thus serving as a central role in the biosphere.<sup>4</sup> In plants, a variety of biochemical, physiological and metabolic pathways require iron as it is an integral part of various enzymes. For instance, iron acts as an important component in the electron transport chain during respiration and photosynthesis, nitrogen fixation,<sup>5</sup> chlorophyll synthesis and DNA synthesis.<sup>6</sup> Iron can be obtained from a variety of dietary sources, including rice, milk, meat, fruits and water. Among vegetables, spinach and broccoli have high iron content. Seafoods such as shellfish and oysters also have a high content of iron.

Concentration of any nutrient below or above a certain level is deleterious,<sup>7</sup> and the same is the case for iron; because it is one of the heavy metals, it can cause toxic effects in living systems and to the environment. It is termed a “heavy metal” on account of its high specific gravity<sup>8</sup> and poisonous effects even at low concentrations.<sup>9</sup> For instance, increased concentration of iron in the body is related to pancreas dysfunction and Alzheimer's disease.<sup>10</sup> Studies have shown that a high level of plasma iron in males is related to an increased risk of coronary artery disease.<sup>11</sup> Hemochromatosis is another condition related to excessive build-up of iron in the liver, skin, joints, pancreas or pituitary gland.<sup>12</sup> Hemochromatosis increases the risk of hepatocellular carcinoma, which is the most common liver malignancy and a leading cause of cancer-related deaths worldwide, by about 100–200 times.<sup>13</sup> The risk of primary liver cancer increases with iron-overloaded states, such as thalassemia, which contribute to both hemochromatosis and hepatocellular carcinoma.<sup>14</sup> Different oxidation states of iron have varying effects on the efficiency of its function, transport, metabolism and toxicity in the body. For instance, the reduced state of iron, Fe<sup>2+</sup>, is responsible for oxygen transport and storage *via* haemoglobin and myoglobin, respectively, while its oxidised state, Fe<sup>3+</sup>, generates methaemoglobin and metmyoglobin, which have no binding capability with oxygen.<sup>15</sup> Another condition related to abnormal iron concentrations in the body is ferroptosis, which refers to the iron-dependent peroxidation of lipids, leading to cell death. The oxidation state of iron is important in ferroptosis as Fe<sup>2+</sup> is linked with lipid peroxidation, while Fe<sup>3+</sup> is inert and is usually stored as ferritin.<sup>16</sup> Therefore, the determination of iron

<sup>a</sup>Department of Chemistry, COMSATS University Islamabad, Abbottabad Campus, University Road, Abbottabad 22060, Pakistan. E-mail: sashahzad@cuiatd.edu.pk

<sup>b</sup>Central Labs, King Khalid University, AlQura'a, P.O. Box 960, Abha, 61413, Saudi Arabia

<sup>c</sup>Department of Chemistry, Faculty of Science, King Khalid University, P.O. Box 9004, Abha 61413, Saudi Arabia

<sup>d</sup>Department of Chemistry, Faculty of Physical Sciences, Government College University Faisalabad, Faisalabad-38000, Pakistan

† Electronic supplementary information (ESI) available. See DOI: <https://doi.org/10.1039/d4ra07824a>


levels along with its oxidation state is important. Currently applied techniques for the detection of iron include capillary electrophoresis,<sup>17</sup> electrochemical sensing,<sup>18</sup> liquid chromatography-mass spectrometry,<sup>19</sup> polarography,<sup>20</sup> voltammetry<sup>21</sup> and atomic absorption spectroscopy.<sup>22</sup> These methods have limited practical applications because of the need for expensive instruments, difficult sample preparation process and limited efficiency. Fluorescence-based detection approach is emerging as an extensively used chemosensing technique because of its high sensitivity and selectivity, quick response time, rapid detection, wide-ranging applications and simplicity.<sup>23–25</sup> Fluorescent sensors offer portability and easy on-site detection of a variety of materials, and hence, they have wide applications in sensing metal ions, pesticides, biomolecules, cancer cells, explosives and dynamite; they even find application in food safety and environmental pollution monitoring.<sup>26–31</sup> Some organic compounds show good emission in the solution form, while their fluorescence emission is reduced upon aggregation due to  $\pi$ - $\pi$  stacking, a phenomenon named aggregation-caused quenching (ACQ).<sup>32,33</sup> Alternatively, some fluorophores have the tendency to show enhanced emission when in the solid form compared to the solution form. This phenomenon is referred to as aggregation-induced emission (AIE).<sup>34</sup> AIE behaviour is observed when some molecular interactions, such as restricted intramolecular rotations (RIRs), motions (RIMs) and vibrations (RIVs), are at play.<sup>35–38</sup> A variety of AIEE-active fluorophores have been developed lately, and they work at fairly low concentrations by showing “turn-on” fluorescence in the aggregated state.<sup>39–41</sup> These AIEE-active fluorophores find practical applications because of their resistance to photobleaching, stability, low signal-to-noise ratio and remarkable Stokes shift.<sup>42,43</sup> Biomedical applications of AIEE-active sensors are attributed to their ability to show minimum or no emission in their solution form but a fairly notable emission in their aqueous solution.<sup>44</sup> Electronic circuits, organic light-emitting diodes (OLEDs) and molecular logic gates also take advantage of the AIEE property of these luminous compounds.<sup>24</sup>

In continuation of the work by our research group<sup>45–52</sup> on the development of novel fluorescent sensors with remarkable selectivity for toxic heavy metals and biologically important compounds, a new fluorescein-based probe **FHP** was developed in this work through a Schiff base reaction for selective detection of  $\text{Fe}^{3+}$ . Probe **FHP** showed AIEE response with manifold-enhanced emission in aqueous media. These remarkable properties of the newly developed probe were used successfully for highly sensitive and selective sensing of  $\text{Fe}^{3+}$ . A detailed study of the photophysical properties and mechanisms involved in  $\text{Fe}^{3+}$  sensing by probe **FHP** was carried out using UV-vis and fluorescence spectroscopy,  $^1\text{H}$  and  $^{13}\text{C}$ -NMR titration experiments and DFT studies to analyse the interactions and support the experimental findings.

## Experimental methods

### Synthesis of FHP

The reaction of fluorescein (332.31 mg, 1.0 mmol) with hydrazine hydrate (2.0 mL) in the presence of ethanol as solvent

afforded fluorescein hydrazine **2**, which was then subjected to a condensation reaction with 2-hydroxyacetophenone under reflux in ethanol for 10 hours in the presence of a few drops of glacial acetic acid, and the progress of the reaction was monitored *via* TLC. After the completion of the reaction, the excess solvent was evaporated, and the residue was purified by extracting it three times in a water-ethyl acetate system. The crude product obtained after solvent extraction was further purified by column chromatography. For column chromatography, silica gel was employed as the stationary phase, while hexane and ethyl acetate served as the mobile phase. The flow rate was adjusted to maintain the steady flow of the liquid mobile phase, and the separation of the desired product was checked by visualizing the TLC plate under a 365 nm UV light. A binary solution of *n*-hexane and ethyl acetate (1 : 1) was run in the column, which provided the purified off-white powder of **FHP**. Yield 78%;  $^1\text{H}$ -NMR (400 MHz,  $\text{DMSO}-d_6$ ):  $\delta$  11.64 (s, 2H), 9.94 (s, 2H, ArH), 7.92 (m, 1H, ArH), 7.62 (m, 3H, ArH), 7.30 (m, 1H), 7.17 (d, 2H,  $J = 7.6$  Hz), 7.07 (t, 1H,  $J = 1.6$  Hz), 6.86 (t, 2H,  $J = 7.5$  Hz), 6.75 (d, 1H,  $J = 8.2$  Hz), 6.59 (m, 4H), 6.51 (m, 3H), 2.28 (s, 3H).  $^{13}\text{C}$ -NMR (100 MHz,  $\text{DMSO}-d_6$ ): ( $\delta$  = ppm): (1  $\times$  C) 17.96, (1  $\times$  C) 66.24, (2  $\times$  C) 102.86, (2  $\times$  C) 109.47, (2  $\times$  C) 113.04, (1  $\times$  C) 112.04, (1  $\times$  C) 117.74, (1  $\times$  C) 118.69, (1  $\times$  C) 119.30, (1  $\times$  C) 123.67, (1  $\times$  C) 124.43, (2  $\times$  C) 129.02, (1  $\times$  C) 129.28, (1  $\times$  C) 129.48, (1  $\times$  C) 129.60, (1  $\times$  C) 130.18, (1  $\times$  C) 133.34, (1  $\times$  C) 134.11, (1  $\times$  C) 151.53, (2  $\times$  C) 152.59, (2  $\times$  C) 159.08, (1  $\times$  C) 159.59, (1  $\times$  C) 161.55, and (1  $\times$  C) 174.70. DEPT-135 NMR (100 MHz,  $\text{DMSO}-d_6$ ): 17.96, (2  $\times$  C) 102.86, (2  $\times$  C) 113.04, 117.74, 134.11, 119.30, 123.67, 124.43, (2  $\times$  C) 129.02, 129.60, 130.18, 133.34.

### UV-visible and fluorescence experiments

The fluorescence spectra of **FHP** (50  $\mu\text{M}$ ) were recorded on a spectrofluorometer using a 1 mM stock solution. The emission spectra of probe **FHP** were observed at 516 nm using an excitation wavelength of 450 nm. Solutions of various analytes (100  $\mu\text{M}$ ) *i.e.*  $\text{Fe}^{3+}$ ,  $\text{Zn}^{2+}$ ,  $\text{K}^+$ ,  $\text{Cu}^{2+}$ ,  $\text{Ca}^{2+}$ ,  $\text{Ag}^+$ ,  $\text{Mg}^{2+}$ ,  $\text{Hg}^{2+}$ ,  $\text{Na}^+$ , and  $\text{Ni}^{2+}$  were scanned against the probe to check its selectivity. The spectral data were recorded with increasing concentrations of  $\text{Fe}^{3+}$  and all the other analytes using a quartz cuvette to record the absorption and emission parameters.

### Computational studies

The proposed  $\text{Fe}^{3+}$  detection mechanism of the synthesised probe **FHP** was further supported by DFT studies, and the simulations were performed on the Gaussian 09 program.<sup>53</sup> For the visualization of results, GaussView 5.0 was used along with Multiwfn 3.7,<sup>54</sup> while the VMD<sup>55</sup> and GaussSum<sup>56</sup> hybrid density function B3LYP (Becke–Lee–Yang–Parr composite of exchange correction functional) method was employed for structure optimization along with the 6-31G(d,p) basis set for mapping C, H, O and N and LANL2DZ<sup>57</sup> for mapping the heavier atom  $\text{Fe}^{3+}$ . The below equation was used to calculate the interaction energy of probe **FHP** with the analyte:

$$E_{\text{int}} = E_{\text{c}} - (E_{\text{p}} + E_{\text{a}}) + E_{\text{BSSE}}$$



where  $E_p$  is the energy of probe **FHP**,  $E_a$  is the analyte energy, and  $E_c$  is complex energy. To study the electronic properties of probe **FHP**, in Gaussian 09 software, frontier molecular orbitals (FMO) and natural bonds orbital (NBO) were investigated. The interaction between probe **FHP** and the analyte was studied by FMO and DOS, which demonstrated the establishment of a new energy band, while the transfer of charge among the interacting moieties of the complex was studied using NBO. The presence of different interacting forces within the interacting moieties, such as electrostatic and van der Waals interactions and repulsive forces due to steric hindrance, was investigated by analysing the non-covalent interactions (NCIs) using VMD and Multiwfn software. The NCI analysis provides an understanding of the 3D isosurface and the 2D reduced density gradient. The below equation illustrates the correlation between the electron density and reduced density gradient (RDG).

$$\text{RDG} = \frac{1}{2(3\pi^2)^{\frac{1}{3}}} \frac{|\nabla\rho(r)|}{\rho(r)^{\frac{4}{3}}}$$

In the above equation, “ $\nabla$ ” is the gradient operator, ( $\rho$ ) indicates the bond strength and  $|\nabla\rho|$  shows the electronic density. To get better insights into the dynamics of the intermolecular interactions of probe **FHP** with analyte  $\text{Fe}^{3+}$ , Bader's QTAIM analysis was performed.<sup>58</sup> The bond critical point (BCP) obtained from QTAIM was used to explore a variety of topological parameters, including Laplacian of electron density  $\nabla^2\rho(r)$ , electron density  $\rho(r)$ , Lagrangian kinetic energy  $G(r)$ , potential energy density  $V(r)$  and energy density  $H(r)$ . All these parameters demonstrated a particular type of bond and the nature of the interaction between probe **FHP** and analyte  $\text{Fe}^{3+}$ .

## Results and discussion

### Synthetic chemistry of probe **FHP**

Fluorescein hydrazine was synthesized *via* condensation reaction, which involved the conversion of the lactone form of fluorescein into its amide form *i.e.* fluorescein hydrazine, with the formation of a water molecule. This condensation reaction was carried out in the ethanol solvent under reflux. Nucleophilic nitrogen from hydrazine attacks the oxygen–acyl bond in fluorescein. In consequence, the lactone ring opens, making oxygen a good leaving group. Oxygen leaves with the protons transferred from hydrazine, and the amide ring is formed. Under similar conditions, probe **FHP** was synthesised in ethanol solvent under reflux *via* a condensation reaction. The amino group in fluorescein hydrazine being nucleophilic in nature attacks on the carbonyl centre of 2-hydroxyacetophenone. This results in the formation of carbinolamine intermediate, and Schiff base **FHP** is formed with the elimination of water (Scheme 1).  $^1\text{H}$ -NMR spectroscopy confirmed the formation of probe **FHP**. The peak of  $\text{NH}_2$  at 4.38 ppm in fluorescein hydrazide disappeared in  $^1\text{H}$ -NMR spectra of **FHP** and new peaks are observed for  $\text{CH}_3$  and the aromatic hydrogens of 2-hydroxyacetophenone. The detailed NMR spectra ( $^1\text{H}$ ,  $^{13}\text{C}$  and DEPT-135 NMR) and information about instrument and reagents are provided in ESI.†



Scheme 1 Synthetic route for probe **FHP**.

### Optimization for emission intensity

After optimization, 50  $\mu\text{M}$  of probe **FHP** in DMF was considered the optimised concentration because it resulted in the maximum intensity and minimum inner filter effect (IFE), as confirmed by the absence of overlapping of the absorption and emission spectra of **FHP** accompanied by a Stokes shift of 190 nm (Fig. S1†). Probe **FHP** displayed the maximum emission at a wavelength ( $\lambda_{\text{max}}$ ) of 516 nm when it was excited using radiation of 450 nm wavelength.

### Water aggregation studies and AIEE characteristics

Some organic compounds show less or no emission in non-polar or organic solvents but become emissive due to aggregation in a solvent of low solubility, such as water.<sup>59</sup> The optical behaviour of probe **FHP** with increasing water content was studied in a binary system (DMF : water). As the concentration of water ( $f_w$ ) was increased from 0–90%, the fluorescence emission intensity of probe **FHP** also increased (Fig. 1a). This significant increase in emission intensity is attributed to the restriction of rotations along the single bonds. This restriction in intramolecular motion causes radiative decay of the molecule, thus leading to enhanced fluorescence emission intensity, contributing to the AIEE characteristics of probe **FHP**. The relative emission intensity plot of the probe against increasing water fractions showed an increase in emission intensity with the water fractions (Fig. 1b). Based on the results, 80%  $f_w$  was selected for further photophysical studies because probe **FHP** showed the maximum intensity in this fraction, demonstrating its practical applicability in biological samples. The polarity of biological systems is in between the polarity of water and organic solvents. Therefore, this mixture provides intermediate polarity that resembles the cellular environment and hence is suitable for studying the possible interactions between molecules. Probe **FHP** showed the highest value of intensity at 90% water, but it was not selected to avoid the maximum emission

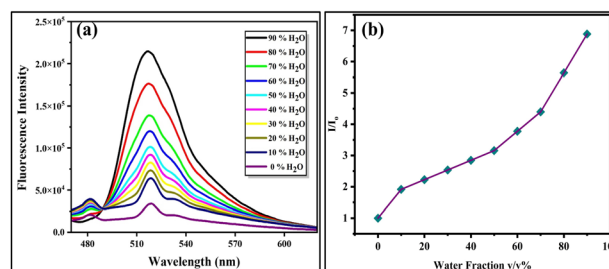


Fig. 1 Emission spectrum of **FHP** with increasing water fraction (0–90%) (a) and relative emission intensity of the probe in increasing water fractions (0–90%) (b).



limit of the spectrofluorometer while maintaining the suitable concentration of the samples.

### Fluorescence sensing of $\text{Fe}^{3+}$

Various biologically important ions were examined in aqueous media ( $\text{H}_2\text{O}/\text{DMF}$ ; 4/1, v/v) through fluorescence titration experiments to investigate the sensing potential of probe **FHP** (50  $\mu\text{M}$ ). Ions that were spiked in the solution of **FHP** for fluorescence studies included  $\text{Fe}^{3+}$ ,  $\text{Zn}^{2+}$ ,  $\text{K}^+$ ,  $\text{Cu}^{2+}$ ,  $\text{Ca}^{2+}$ ,  $\text{Ag}^+$ ,  $\text{Mg}^{2+}$ ,  $\text{Hg}^{2+}$ ,  $\text{Na}^+$  and  $\text{Ni}^{2+}$ . A selective quenching response of probe **FHP** was observed with the gradual increase in the concentration of  $\text{Fe}^{3+}$ . The response of probe **FHP** towards analytes other than  $\text{Fe}^{3+}$  was insignificant, demonstrating the selective behaviour of probe **FHP** towards  $\text{Fe}^{3+}$  only (Fig. 2a).

A strong fluorescence emission at 516 nm was observed for probe **FHP**. When probe **FHP** was titrated only against  $\text{Fe}^{3+}$  from 0–100  $\mu\text{M}$ , the emission intensity of **FHP** decreased gradually with increasing concentrations of  $\text{Fe}^{3+}$  (Fig. 2b). A 2D Stern–Volmer plot was drawn to illustrate the binding efficacy of **FHP** with  $\text{Fe}^{3+}$ , which displayed a continuous upward trend. The Stern–Volmer constant was calculated using the equation given below, which further verified the sensitivity of probe **FHP** to  $\text{Fe}^{3+}$  (Fig. 2c).

$$I_0/I = 1 + K_{\text{sv}}[Q]$$

In the above equation,  $I_0$  is the emission intensity before the addition of  $\text{Fe}^{3+}$ , while  $I$  is the intensity of emission after the addition of  $\text{Fe}^{3+}$ .  $K_{\text{sv}}$  represents the Stern–Volmer constant, and  $[Q]$  indicates the concentration of the quenching agent *i.e.*  $\text{Fe}^{3+}$ . Probe **FHP** showed maximum quenching for 100  $\mu\text{M}$   $\text{Fe}^{3+}$ . The relative intensity  $I_0/I$  was plotted against increasing

concentrations of  $\text{Fe}^{3+}$  to construct the Stern–Volmer plot.  $8.0 \times 10^4 \text{ M}^{-1}$  was the value of the Stern–Volmer constant  $K_{\text{sv}}$ . The limit of detection (LOD) was calculated to be 253 nM using the formula  $3\sigma/S$ , which estimates the level of sensitivity of probe **FHP** towards  $\text{Fe}^{3+}$  from the Stern–Volmer plot in the concentration range of 0–10  $\mu\text{M}$  (Fig. S2†). The measured value of the LOD of probe **FHP** is greater than those of previously reported  $\text{Fe}^{3+}$  probes (Table S1†).

### Probable sensing mechanism

The plausible mechanism of fluorescence sensing was investigated based on the experimental results obtained. The sensing mechanism of  $\text{Fe}^{3+}$  ions by the **FHP** probe was evaluated by performing  $^1\text{H}$ -NMR titration experiments to elucidate whether the interaction was covalent or non-covalent in nature. For this purpose,  $^1\text{H}$ -NMR spectra were obtained by dissolving 1:1 equivalents of **FHP** and  $\text{Fe}^{3+}$  in the  $\text{DMSO}-d_6$  solvent.

The degree of change in the chemical shift, multiplicity and integration gives information about the interaction type. The appearance of new peaks, significant changes in the chemical shift ( $\delta$ ) or multiplicity and integration change can demonstrate covalent interactions between the probe and the analyte. However, in the case of the **FHP**– $\text{Fe}^{3+}$  complex, neither a new peak appeared nor a change in the integration or multiplicity was observed. Only a negligible shift in the spectral peaks from 11.64, 9.95 and 7.93 in **FHP** to 11.60, 9.93 and 7.89, respectively, in **FHP**– $\text{Fe}^{3+}$  complex was observed, clearly demonstrating the presence of non-covalent type interaction between probe **FHP** and  $\text{Fe}^{3+}$  (Fig. 3a). Furthermore, the fluorescence titration experiments of **FHP** and  $\text{Fe}^{3+}$  showed quenching of the emission intensity of the **FHP** probe upon interaction with increasing concentrations (0–100  $\mu\text{M}$ ) of  $\text{Fe}^{3+}$  ions. No new peak

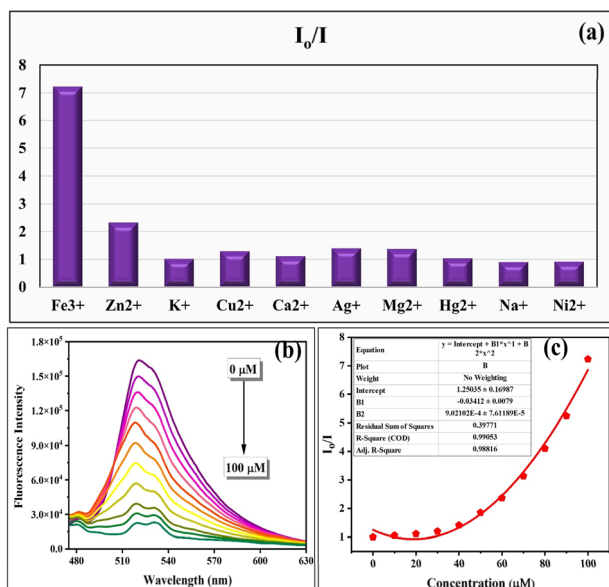


Fig. 2 Relative emission of **FHP** in the presence of different analytes (100  $\mu\text{M}$ ) (a). Fluorescence emission of **FHP** with increasing  $\text{Fe}^{3+}$  concentrations (0–100  $\mu\text{M}$ ) in  $\text{H}_2\text{O}/\text{DMF}$  (4/1, v/v) system (b) and Stern–Volmer plot of **FHP** against  $\text{Fe}^{3+}$  (0–100  $\mu\text{M}$ ) (c).

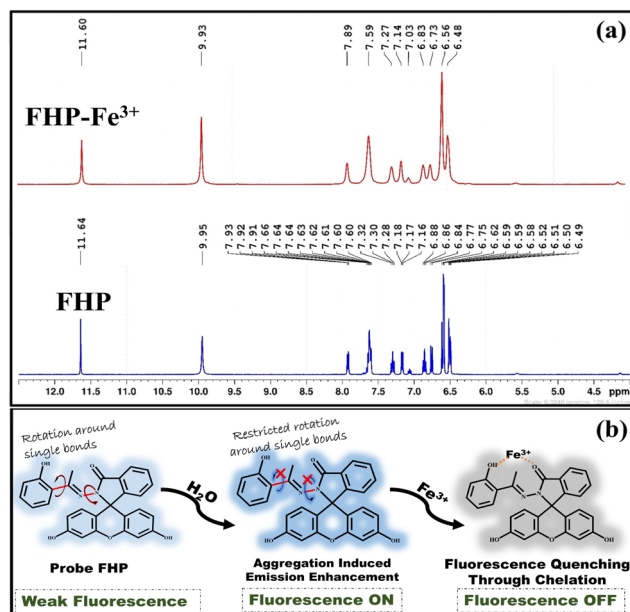


Fig. 3  $^1\text{H}$ -NMR (400 MHz,  $\text{DMSO}-d_6$ ) titration spectra of <



appeared in the emission spectra, further verifying the non-covalent type interaction between the **FHP** probe and  $\text{Fe}^{3+}$  ions. Similar behaviour was also observed in UV-vis titration experiments. Only quenching was observed without the generation of new peaks (Fig. S3†). The absence of new peaks in both the UV and emission spectra illustrates that ICT is not responsible for quenching the **FHP** molecule upon interaction with  $\text{Fe}^{3+}$ .  $\text{Fe}^{3+}$  is a well-known fluorescence quencher that is electron deficient and can accept electrons from electron-rich atoms. The carbonyl and hydroxyl groups present at the terminal ends of probe **FHP** make it an electron-rich entity that can donate electrons to the metal  $\text{Fe}^{3+}$  ions. Therefore, probe **FHP** might have chelated the  $\text{Fe}^{3+}$  metal ions, which in turn opens the non-radiative decay pathway, due to which the fluorescence emission intensity of **FHP** reduces during interaction with  $\text{Fe}^{3+}$  ions (Fig. 3b). Moreover, the binding stoichiometry was calculated by Job's plot, which validated the binding capability of probe **FHP** with  $\text{Fe}^{3+}$ . By varying the mole fraction from 0 to 1, different concentrations of probe **FHP** and  $\text{Fe}^{3+}$  were utilized to construct the Job's plot. The binding stoichiometry of 1 : 1, which depicts the binding of one molecule of **FHP** with one ion of  $\text{Fe}^{3+}$ , yielded the maximum relative emission intensity value at 0.5 mole fraction (Fig. S4†). In addition to this, the DLS analysis results also verified the binding of **FHP** with  $\text{Fe}^{3+}$  based on the increase in particle size of **FHP** from 323.3 nm to 520.4 nm (Fig. S5†). During the interaction between the AIEE-active probe and the analyte,  $\text{Fe}^{3+}$  gets into the layers of the aggregates of probe **FHP**, and due to complex formation, the overall size appears to increase. Moreover, the presence of non-covalent interactions between **FHP** and  $\text{Fe}^{3+}$  and the charge transfer from **FHP** to  $\text{Fe}^{3+}$  were theoretically supported by DFT studies, in which the non-covalent interactions were visualised through NCI analysis, and the numerical value of charge transfer was calculated by NBO analysis, which showed that 1.01823  $e^-$  charge was transferred from **FHP** to  $\text{Fe}^{3+}$ .

### Interference studies

To investigate the selectivity of **FHP**, sensing studies were carried out in the presence of different interfering analytes, including  $\text{K}^+$ ,  $\text{Cu}^{2+}$ ,  $\text{Ca}^{2+}$ ,  $\text{Ag}^+$ ,  $\text{Mg}^{2+}$ ,  $\text{Hg}^+$ ,  $\text{Na}^+$ ,  $\text{Ni}^+$ ,  $\text{NO}^{3+}$ ,  $\text{Cl}^-$ ,  $\text{CN}^-$ ,  $\text{H}_2\text{O}_2$ , and  $\text{N}_2\text{H}_4$ . The fluorescence response of probe **FHP** was unaffected in the presence of interfering species and remained selective for  $\text{Fe}^{3+}$  (Fig. S6†). The sensing capability of **FHP** was investigated under varying pH conditions ranging from 3–11 to explore its applicability for on-site detection. Despite changing pH, the quenching response of probe **FHP** by  $\text{Fe}^{3+}$  was unaffected (Fig. S7a†). The effect of temperature was also studied by changing the temperature from 20–60 °C in a DMF:water system. The temperature was not increased to 100 °C to avoid boiling of water. The sensing response of **FHP** remained unaffected with increasing temperatures (Fig. S7b†). The quenching response of **FHP** was observed, and the quenching efficiency remained constant for  $\text{Fe}^{3+}$  from 20–60 s, demonstrating the quick response time of probe **FHP** (Fig. S8a†). A photostability test was carried out, and probe **FHP** was exposed to high-energy radiations. Probe **FHP** was fairly

stable and showed no fluctuations in  $\text{Fe}^{3+}$  sensing capability (Fig. S8b†). Probe **FHP** was found suitable for practical use as its fluorescence response was independent of pH changes, varying temperature and photobleaching and it showed a quick response time.

### DFT studies

**Interaction energy and NBO analysis.** For thermodynamic studies, the  $\omega\text{B97XD}/6\text{-}31\text{G(d,p)}$  functional was incorporated to investigate the energy of interaction ( $E_{\text{in}}$ ) between probe **FHP** and  $\text{Fe}^{3+}$ . The value of ( $E_{\text{in}}$ ) is linked directly to the thermodynamic stability. A greater  $E_{\text{in}}$  value reflects greater thermodynamic stability.<sup>60,61</sup> The optimized geometry of **FHP**– $\text{Fe}^{3+}$  has an  $E_{\text{in}}$  of 647.74 kcal mol<sup>−1</sup> based on BSSE calculations (Fig. S9†). The natural bond orbital (NBO) charge analysis was performed to determine the numerical value of charge transfer from **FHP** to  $\text{Fe}^{3+}$  during their interaction. A total charge of 1.01823  $e^-$  was transferred from **FHP** to  $\text{Fe}^{3+}$ , which depicts that  $\text{Fe}^{3+}$  possessed good electron acceptance characteristics.  $\text{Fe}^{3+}$  can bind to the electron-rich centre of **FHP**, establishing the **FHP**– $\text{Fe}^{3+}$  interaction.

**Electronic features.** Molecular orbital analysis was performed to determine the energies of the highest occupied (HOMO) and lowest unoccupied (LUMO) orbitals of probe **FHP** and the **FHP**– $\text{Fe}^{3+}$  complex. Furthermore, the numerical values of the energy gaps of both probe **FHP** and complex **FHP**– $\text{Fe}^{3+}$  were determined to justify the detection of  $\text{Fe}^{3+}$  by **FHA**. The energies of HOMO and LUMO of isolated **FHP** were −4.77 eV and −0.88 eV, respectively. There was a prominent decrease in the energy gap of the pure probe from 3.89 eV to 1.97 eV in the **FHP**– $\text{Fe}^{3+}$  complex, indicating strong interaction, overlapping of the **FHP** and  $\text{Fe}^{3+}$  orbitals and greater sensitivity. Similarly, the DOS spectra give insights into the changes in electronic properties after complexation with  $\text{Fe}^{3+}$ . Similar observations were drawn from the DOS spectra. A reduction in the energy gap of the highest occupied and virtual orbitals and the appearance

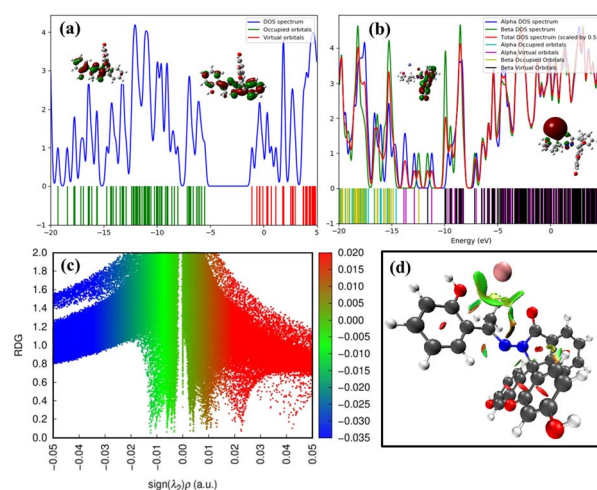


Fig. 4 FMO and DOS spectra of probe **FHP** (a) and **FHP**– $\text{Fe}^{3+}$  complex (b), 2D NCI (c) and 3D isosurface graphics of **FHP**– $\text{Fe}^{3+}$  (d).



Table 1 BCP parameters of the FHP-Fe<sup>3+</sup> complex

BCPs	FHA-Fe <sup>3+</sup>	$\rho(r)$ (a.u.)	$\nabla^2\rho(r)$ (a.u.)	$G(r)$ (a.u.)	$V(r)$ (a.u.)	$H(r)$ (a.u.)	$-V/G$	$E_{\text{int}}$ (kcal mol <sup>-1</sup> )
1	O...Fe <sup>3+</sup>	0.004	0.008	0.002	-0.002	-0.001	1.00	0.627
2	C...Fe <sup>3+</sup>	0.006	0.016	0.004	-0.005	-0.0004	1.25	1.56
3	O...Fe <sup>3+</sup>	0.003	0.006	0.001	-0.002	-0.0003	2.00	0.627

of new spectral peaks in the FHP-Fe<sup>3+</sup> complex clearly illustrated the interaction of Fe<sup>3+</sup> with FHP (Fig. 4a and b).

**Non-covalent interaction (NCI) and QTAIM analysis.** NCI is a viable approach based on the density gradient and reduced density gradient to obtain information about the type of interactions, such as van der Waals interactions, hydrogen bonds, and steric hindrance, in complexes. The type of interactions responsible for Fe<sup>3+</sup> sensing by FHP was further visualised and verified using NCI 3D and 2D graphical abstracts. The dotted green lines in the 2D spectrum indicate the van der Waals interactions between Fe<sup>3+</sup> and the terminal oxygen atoms of FHP, while the red falling spikes illustrate repulsions that exist between the rings of FHP molecules (Fig. 4c). Further, the big green contour between Fe<sup>3+</sup> and FHP and the small red spots between the rings of FHP justify these results (Fig. 4d). In addition to this, QTAIM analysis was carried out to further illustrate the actual interacting atoms in probe FHP and Fe<sup>3+</sup> in the form of 3 bond critical points (BCPs) between Fe<sup>3+</sup> and the highly electronegative atoms of FHP (Fig. 5a and Table 1).

### Practical applications

**Detection of Fe<sup>3+</sup> in biological samples.** Detection of Fe<sup>3+</sup> in biological samples was examined using a spectrofluorometer, and the emission of probe FHP was recorded in the presence of different Fe<sup>3+</sup> concentrations. For this purpose, blood samples were collected from the Ayub Medical Complex Hospital. These blood samples were subjected to centrifugation so that the plasma and blood cells were separated. These samples were incubated for 5 hours after the addition of 50  $\mu$ M probe. After incubation, the samples were spiked with Fe<sup>3+</sup> (0–50  $\mu$ M).

The fluorescence spectra of probe FHP showed efficient fluorescence quenching response in the plasma samples with increasing concentrations of Fe<sup>3+</sup> (Fig. 5b). A calibration curve was drawn to compare the results of biological samples with the lab samples (Fig. S10<sup>†</sup>), and the calculated recovery percentages

were between 96.5% and 105% (Table S2<sup>†</sup>). This shows that FHP exhibits quenching behaviour in the presence of Fe<sup>3+</sup> and can be used for Fe<sup>3+</sup> detection in biological samples.

**Solid state detection.** To test the practical applicability of probe FHP for the detection of Fe<sup>3+</sup> in solid-state samples, solid-state fluorescence spectroscopy was performed using a spectrofluorometer. Probe FHP (50  $\mu$ M) was coated on a filter paper, dried and placed in the spectrophotometer. The initial fluorescence spectrum of the probe was recorded, and after applying different concentrations of Fe<sup>3+</sup>, the filter paper was again scanned. Noticeable quenching was observed with increasing Fe<sup>3+</sup> concentrations (0–100  $\mu$ M). This shows that FHP could sense Fe<sup>3+</sup> even in the solid state (Fig. S11<sup>†</sup>).

## Conclusion

A fairly good yield (78%) of FHP was obtained under simple and convenient reaction conditions. FHP was then developed as a probe for the detection of Fe<sup>3+</sup>. FHP displayed AIEE properties with increasing  $f_w$  in a DMF : water (1 : 4, v/v) system with a  $\lambda_{\text{max}}$  of 516 nm. FHP could effectively sense Fe<sup>3+</sup> ions with an LOD of 253 nM. The <sup>1</sup>H and <sup>13</sup>C titration NMR results justified the presence of non-covalent interactions. The Job's plot of FHP displayed a binding stoichiometry of 1 : 1 with Fe<sup>3+</sup>. Furthermore, DLS showed that the particle size of the FHP-Fe<sup>3+</sup> complex was 520.3 nm and that of the FHP probe was 323.4 nm. Quenching of FHP fluorescence emission intensity in the presence of Fe<sup>3+</sup> could be attributed to the chelation between the electron-rich centre of FHP and electron-deficient Fe<sup>3+</sup>. Probe FHP was able to successfully sense Fe<sup>3+</sup> in the presence of various interfering species, varying pH ranges and even temperature changes, demonstrating excellent sensitivity and selectivity towards FHP. Solid-state fluorescence spectroscopy provided insights into the solid-state detection of Fe<sup>3+</sup> by FHP. On exposure to high-energy radiations, FHP remained perfectly stable. In electronic analysis, a reduction in the HOMO–LUMO gap from 3.89 eV to 1.97 eV and the appearance of a new virtual energy peak provided evidence of the great sensitivity of FHP for Fe<sup>3+</sup>. The NCI analysis indicated non-covalent interactions between FHP and Fe<sup>3+</sup>, and QTAIM analysis further elucidated those three interacting points as BCPs. FHP could even sense Fe<sup>3+</sup> in real biological samples with remarkable efficacy, which exemplifies its potential for practical usage in the real world.

## Data availability

The data supporting this article have been included as part of the ESI.<sup>†</sup>

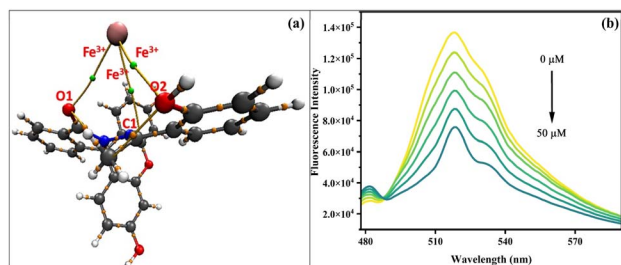


Fig. 5 QTAIM analysis of FHP-Fe<sup>3+</sup> (a) and fluorescence spectra of FHP in biological samples (0–50  $\mu$ M) (b).



## Author contributions

Rida Khalid: methodology, investigation, validation, writing – original draft. Tayyeba Javid: methodology, investigation, formal analysis, writing – original draft. Aqsa Pervaiz: investigation, methodology, software. Mohammed A. Assiri: visualization, methodology, investigation, funding acquisition. Zulfiqar Ali Khan: investigation, visualization. Sania: methodology. Sohail Anjum Shahzad: supervision, conceptualization, methodology, visualization, validation, investigation, project administration, funding acquisition, writing – review & editing.

## Conflicts of interest

The authors declare that they have no known competing financial interests or personal relationships that could have appeared to influence the work reported in this paper.

## Acknowledgements

The authors extend their appreciation to University Higher Education Fund for funding this research work under Research Support Program for Central Labs at King Khalid University through the project number CL/PRI/RP/10.

## Notes and references

- 1 D. Meynard, J. L. Babitt and H. Y. Lin, *Blood*, 2014, **123**, 168–176.
- 2 V. K. Gupta, A. Jain, S. Agarwal and G. Maheshwari, *Talanta*, 2007, **71**, 1964–1968.
- 3 G. R. Rout and S. Sahoo, *Rev. Agric. Sci.*, 2015, **3**, 1–24.
- 4 F. A. Cotton, G. Wilkinson, C. A. Murillo and M. Bochmann, *Advanced inorganic chemistry*, John Wiley & Sons, 6th edn, 1999.
- 5 J. Kim and D. Rees, *Science*, 1992, **257**, 1677–1682.
- 6 S. Puig, L. Ramos-Alonso, A. M. Romero and M. T. Martínez-Pastor, *Metallomics*, 2017, **9**, 1483–1500.
- 7 R. Bharti and R. Sharma, *Mater. Today: Proc.*, 2022, **51**, 880–885.
- 8 K. J. Appenroth, *Acta Physiol. Plant.*, 2010, **32**, 615–619.
- 9 R. K. Sharma and M. Agrawal, *J. Environ. Biol.*, 2005, **26**, 301–313.
- 10 A. Y. A. Alzahrani, K. O. Khan, S. Rafique, H. Irshad, Khadija, A. M. Khan and S. A. Shahzad, *Spectrochim. Acta, Part A*, 2023, **297**, 122745.
- 11 Z. Li, X. Li, Y. Zhang, X. Feng, F. Yang, D. Su, J. Qiu, W. Ling and Y. Yang, *Food Funct.*, 2013, **4**, 1535–1542.
- 12 J. Balogh, D. Victor III, E. H. Asham, S. G. Burroughs, M. Boktour, A. Saharia, X. Li, R. M. Ghobrial and H. P. Monsour Jr, *J. Hepatocell. Carcinoma*, 2016, 41–53.
- 13 C. Ko, N. Siddaiah, J. Berger, R. Gish, D. Brandhagen, R. K. Sterling, S. J. Cotler, R. J. Fontana, T. M. McCashland and S. H. Han, *Liver Int.*, 2007, **27**, 1394–1401.
- 14 K. Hino, I. Yanatori, Y. Hara and S. Nishina, *FEBS J.*, 2022, **289**, 7810–7829.
- 15 A. Safavi and H. Abdollahi, *Microchem. J.*, 1999, **63**, 211–217.
- 16 T. Chen, L. Liang, Y. Wang, X. Li and C. Yang, *Apoptosis*, 2024, **29**, 289–302.
- 17 H. J. Lin, K. P. Hsieh, S. S. Chiou, H. S. Kou and S. M. Wu, *J. Pharm. Biomed. Anal.*, 2016, **131**, 497–502.
- 18 J. W. Oh, T. H. Kim, S. W. Yoo, Y. O. Lee, Y. Lee, H. Kim, J. Kim and J. S. Kim, *Sens. Actuators, B*, 2013, **177**, 813–817.
- 19 M. Y. Lu, N. Wang, W. H. Wu, C. W. Lai, P. H. Kuo, P. H. Chiang, K. H. Lin and T. H. Wu, *Clin. Ther.*, 2015, **37**, 1751–1760.
- 20 S. Wang, L. Du, A. Zhang and B. Li, *Anal. Lett.*, 1997, **30**, 2099–2107.
- 21 A. Bobrowski, K. Nowak and J. Zarebski, *Anal. Bioanal. Chem.*, 2005, **382**, 1691–1697.
- 22 A. Ohashi, H. Ito, C. Kanai, H. Imura and K. Ohashi, *Talanta*, 2005, **65**, 525–530.
- 23 S. Xia, S. Y. Xiao, Q. Q. Hong, J. R. Zou, S. Yang, M. X. Zhang and H. Zuo, *RSC Adv.*, 2015, **5**, 5244–5249.
- 24 Khadija, H. Irshad, S. Rafique, A. M. Khan, S. Nawazish, H. ur Rehman, M. Imran, S. A. Shahzad and U. Farooq, *Spectrochim. Acta, Part A*, 2023, **290**, 122273.
- 25 S. Rafique, A. Y. A. Alzahrani, Khadija, H. Irshad, A. M. Khan and S. A. Shahzad, *Spectrochim. Acta, Part A*, 2023, **300**, 122946.
- 26 J. H. Jung, D. S. Cheon, F. Liu, K. B. Lee and T. S. Seo, *Angew. Chem., Int. Ed.*, 2010, **49**, 5708–5711.
- 27 A. Majeed, M. A. Assiri, H. Irshad, Khadija, M. Z. Ullah and S. A. Shahzad, *Microchem. J.*, 2024, **201**, 110640.
- 28 K. O. Khan, M. A. Assiri, H. Irshad, S. Rafique, A. M. Khan, A. K. Khan, M. Imran and S. A. Shahzad, *J. Photochem. Photobiol., A*, 2023, **442**, 114805.
- 29 H. Irshad, Khadija and K. Qvortrup, *J. Mol. Liq.*, 2024, 126049.
- 30 M. A. Assiri, S. Hanif, H. M. Junaid, A. Hamad, H. Irshad, M. Yar, W. Rauf and S. A. Shahzad, *J. Photochem. Photobiol., A*, 2023, **438**, 114514.
- 31 A. Pervaiz, S. A. Shahzad, M. A. Assiri, T. Javid, H. Irshad and K. Qvortrup, *J. Hazard. Mater. Lett.*, 2024, **5**, 100132.
- 32 W. Z. Yuan, P. Lu, S. Chen, J. W. Lam, Z. Wang, Y. Liu, H. S. Kwok, Y. Ma and B. Z. Tang, *Adv. Mater.*, 2010, **22**, 2159–2163.
- 33 J. Qi, X. Hu, X. Dong, Y. Lu, H. Lu, W. Zhao and W. Wu, *Adv. Drug Delivery Rev.*, 2019, **143**, 206–225.
- 34 J. Zhang, H. Zhang, J. W. Lam and B. Z. Tang, *Chem. Res. Chin. Univ.*, 2021, **37**, 1–15.
- 35 M. Kang, Z. Zhang, N. Song, M. Li, P. Sun, X. Chen, D. Wang and B. Z. Tang, *Aggregate*, 2020, **1**, 80–106.
- 36 S. Liu, G. Feng, B. Z. Tang and B. Liu, *Chem. Sci.*, 2021, **12**, 6488–6506.
- 37 R. Abassi, F. Abassi, A. Mosavizadeh, H. Sadeghi and A. Keshtkari, *Journal of Clinical Care and Skills*, 2020, **1**, 127–132.
- 38 M. A. Assiri, F. Munir, M. T. Waseem, H. Irshad, W. Rauf and S. A. Shahzad, *Microchem. J.*, 2023, **193**, 109220.
- 39 X. Sun, B. M. Chapin, P. Metola, B. Collins, B. Wang, T. D. James and E. V. Anslyn, *Nat. Chem.*, 2019, **11**, 768–778.
- 40 T. Javid, M. A. Assiri, A. Pervaiz, H. Irshad, K. Qvortrup and S. A. Shahzad, *J. Mol. Liq.*, 2024, **409**, 125526.



- 41 M. A. Assiri, S. Rafique, H. Irshad, Z. A. Khan, F. A. Khan and S. A. Shahzad, *J. Mol. Struct.*, 2024, **1307**, 137963.
- 42 J. Yang, Z. Chi, W. Zhu, B. Z. Tang and Z. Li, *Sci. China:Chem.*, 2019, **62**, 1090–1098.
- 43 N. Jiang, T. Shen, J. Z. Sun and B. Z. Tang, *Sci. China Mater.*, 2019, **62**, 1227–1235.
- 44 Z. Liu, Q. Wang, W. Qiu, Y. Lyu, Z. Zhu, X. Zhao and W. H. Zhu, *Chem. Sci.*, 2022, **13**, 3599–3608.
- 45 K. Khurshid, S. A. Shahzad, M. A. Assiri, A. Shabbir, T. Javid and H. Irshad, *RSC Adv.*, 2024, **14**, 21682–21691.
- 46 H. Rabale, H. Irshad, A. Pervaiz, S. S. Almujri, A. Y. A. Alzahrani, M. Z. Ullah and S. A. Shahzad, *Microchem. J.*, 2024, **205**, 111312.
- 47 R. Khalid, S. A. Shahzad, M. A. Assiri, T. Javid, H. Irshad and M. Z. Ullah, *Microchem. J.*, 2024, **200**, 110264.
- 48 I. Ullah, S. A. Shahzad, M. A. Assiri, M. Z. Ullah, H. Irshad and U. Farooq, *Spectrochim. Acta, Part A*, 2024, **314**, 124224.
- 49 A. Pervaiz, S. A. Shahzad, M. A. Assiri, T. Javid, H. Irshad and K. O. Khan, *Spectrochim. Acta, Part A*, 2024, **313**, 124121.
- 50 M. Z. Ullah, S. A. Shahzad, M. A. Assiri, H. Irshad, S. Rafique, S. A. Shakir and A. Mumtaz, *Spectrochim. Acta, Part A*, 2024, **306**, 123607.
- 51 T. Javid, S. A. Shahzad, M. A. Assiri, A. Pervaiz, Khadija and H. Irshad, *Microchem. J.*, 2024, **199**, 109934.
- 52 S. Rafique, H. Irshad, S. Majeed, Khadija, R. Rubab, M. Imran, A. M. Khan and S. A. Shahzad, *J. Photochem. Photobiol., A*, 2023, **437**, 114459.
- 53 M. Biczysko, P. Panek, G. Scalmani, J. Bloino and V. Barone, *J. Chem. Theory Comput.*, 2010, **6**, 2115–2125.
- 54 T. Lu and F. Chen, *J. Comput. Chem.*, 2012, **33**, 580–592.
- 55 W. Humphrey, A. Dalke and K. Schulten, *J. Mol. Graphics*, 1996, **14**, 33–38.
- 56 N. M. O'boyle, A. L. Tenderholt and K. M. Langner, *J. Comput. Chem.*, 2008, **29**, 839–845.
- 57 P. J. Hay and W. R. Wadt, *J. Chem. Phys.*, 1985, **82**, 270–283.
- 58 R. Bader, *Acc. Chem. Res.*, 1985, **18**, 9.
- 59 H. Tian Jr, A. C. Sedgwick, H. H. Han, S. Sen, G.-R. Chen, Y. Zang, J. L. Sessler, T. D. James, J. Li and X. P. He, *Coord. Chem. Rev.*, 2021, **427**, 213577.
- 60 M. Sohail, F. Khaliq, T. Mahmood, K. Ayub, S. Tabassum and M. A. Gilani, *Radiat. Phys. Chem.*, 2021, **184**, 109457.
- 61 X. Quan, X. Xu and B. Yan, *J. Hazard. Mater.*, 2022, **427**, 127869.

